CORRELATION OF SIDESCAN SONAR ACOUSTIC SHADOWS AND BATHYMETRY FOR TERRAIN-RELATIVE NAVIGATION

Jose Padial*
jpadial@stanford.edu

Shandor G. Dektor*
sgd@stanford.edu

Stephen M. Rock*†
rock@stanford.edu

*Aerospace Robotics Laboratory, Stanford University
496 Lomita Mall, Rm 250, Stanford, CA 94305, USA
†Monterey Bay Aquarium Research Institute (MBARI)
7700 Sandholdt Road, Moss Landing, CA 95039, USA

***Abstract*—This paper explores the feasibility of incorporating non-interferometric sidescan sonar data into a Terrain-Relative Navigation (TRN) filter. Standard TRN methods using downward-looking ranging sensors work well in general, but can lose accuracy when flying over terrain low in information, i.e. flat. The incorporation of side-looking information could potentially augment TRN performance in locally flat terrain. Sidescan sonar is chosen for incorporating side-looking information due to its low cost, low power and because is it a sensor commonly found on AUVs. Specifically, a method is presented to correlate acoustic shadows in a measured sidescan signal with shadows predicted based on the bathymetry map. These acoustic shadows are significant drops in the sidescan sonar intensity signal in the time-of-flight data. Results are presented using field data from Monterey Bay Aquarium Research Institute (MBARI) *Dorado*-class AUV runs that demonstrate the viability of using sidescan sonar acoustic shadow information for TRN.**

I. Introduction

Terrain-Relative Navigation (TRN) is an emerging technology for localization of autonomous underwater vehicles (AUVs). TRN solutions rely on the correlation of a bathymetric terrain map with downward-looking range measurements, for example the four ranging beams of a doppler velocity log (DVL). TRN has been demonstrated successfully in the field with meter-level accuracy [1], however, when flying over terrain low in information, i.e. flat, TRN accuracy can be degraded [2].

The incorporation of side-looking information holds the potential to augment TRN performance over flat terrain. Specifically, if there is bathymetric information port or starboard, fusing side-looking information with standard downward-looking measurements could enable a more accurate navigation estimate. While there are multiple sensors that could measure these side-looking data, including multibeam sonars, interferometric sidescan sonars as in [3], and non-interferometric sidescan sonars, this paper focuses on the use of non-interferometric sidescan sonars because they are ubiquitous in the AUV community, and are comparatively less expensive and lower power than multibeam sonars and interferometric sidescan sonars.

This paper demonstrates the feasibility of non-interferometric sidescan sonar as a sensor for TRN. Navigation results are presented using AUV field data that demonstrate TRN performance using sidescan sonar data comparable to DVL-based TRN. Specifically, methods to correlate sidescan sonar signals with a bathymetric terrain map for aid in TRN by exploiting acoustic shadow data are presented. Acoustic shadows are significant drops in sidescan sonar intensity signal in the time of flight domain. Figure 1 shows starboard

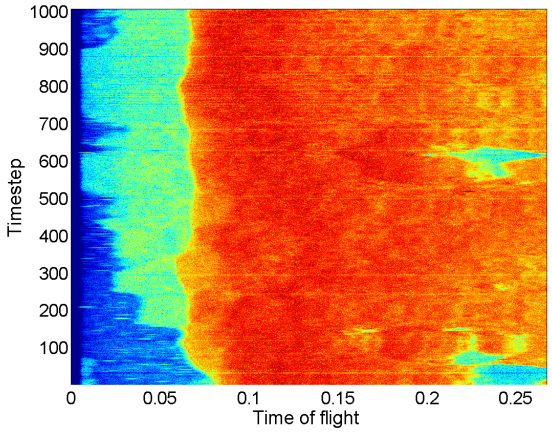

(a) Sidescan sonar image (starboard)

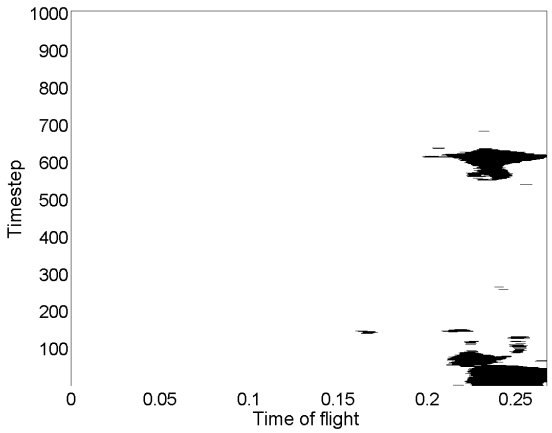

(b) Acoustic shadows

Figure 1: Sidescan sonar image and acoustic shadows. (a) The starboard sidescan image is composed of return intensities for measured time of flight, stacked vertically across multiple measurements made over a run of roughly 500m distance travelled. (b) The acoustic shadows, shown in black, are large drops in intensity, and are extracted by thresholding.

sidescan sonar signals accumulated over roughly 500m of vehicle distance travelled, along with identified acoustic shadows.

A. Sidescan Sonar Returns

Sidescan sonar operates by emitting a single pulse of acoustic energy into the water column, then listening for return signal, as illustrated by Figure 2. Sidescan sonar data comprise return intensities for time of flight values, as opposed to range in given beam directions as with a multibeam sonar or DVL. As such, there is an unavoidable ambiguity in extrapolating spatial information from sidescan sonar data, and some assumption, e.g. flat bottom, must be made in order to do so.

Sidescan sonar data is primarily used in the context of sidescan imagery. These images are often used for detection of man-made objects on the seafloor, e.g. pipelines, ships, or mines as in [4].

To incorporate sidescan sonar data into a TRN filter, a measurement model must be defined that takes as inputs a map and expected vehicle pose and outputs an expected sensor signal, which can then be correlated with a measured sensor signal. Forming a measurement model for sidescan sonar intensity return values is difficult, as sidescan intensity returns are complex functions of grazing angle, terrain surface composition, and water properties [5]. Further, there are gains and filters applied to the raw signal internal to the sensor which are often, as is the case with this work, unknown to the operator. As such, predicting the intensity signal accurately requires more than a vehicle pose estimate and bathymetry map alone. *Acoustic shadows* in the intensity signal, however, are determined primarily by line of sight occlusion due to the geometry of ensonified terrain relative to the sonar transducer, and are subsequently well-suited to bathymetry-based correlation techniques.

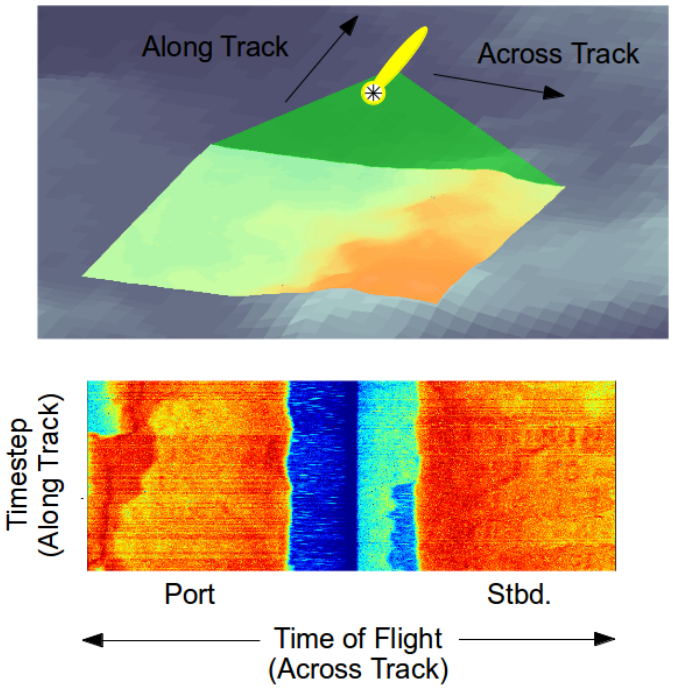

Figure 2: Sidescan sonar acoustic pulse and return diagram. The top diagram depicts a single pulse of acoustic energy (green) emitted at a given timestep. Intensity returns are recorded by time of flight and stitched together vertically to produce the sidescan sonar *time of flight* image shown in the lower diagram. Blue indicates low intensity returns in the sidescan image. The low return area in the middle of the sidescan image denotes the minimum time of flight returns according to the AUV altitude and minimum return angle. Note: the horizontal axis is time of flight, unlike the usual display in distance (e.g. meters) when a flat bottom assumption has been employed.

II. Related Work

Sidescan sonar returns have been successfully utilized in navigation solutions in the past, however these solutions differ from the approach presented in this paper. Some work has focused on the use of sidescan images to eliminate navigation drift by matching sidescan image features across multiple sidescan images, assuming a flat seafloor to extrapolate spatial information from sidescan returns. For example, in [6] a method is proposed to detect and match landmarks in sidescan imagery by level set evolution on Haralick feature maps, where the nature of the landmark registration is similar in nature to visual feature matching. Also, the work of Fallon et al. [7] matched sidescan image features across multiple sidescan images and fused the spatial matching with acoustic ranging from a surface vessel for navigation drift mitigation.

In a similar vein, sidescan sonar has been used in AUV Simulataneous Localization and Mapping (SLAM) solutions in the context of landmark detection and matching for improved navigation. In [8], distinctive features are identified in the sidescan sonar imagery, and matched across images to estimate and track landmark positions. These landmark correspondences are used to improve the navigation estimate in order to project a more smooth and consistent sidescan map. Once again, a flat bottom assumption was necessary in order to extrapolate spatial information from sidescan sonar returns.

The work presented in this paper differs from these past works in that the presented method produces a navigation estimate with respect to an *a priori* terrain map, rather than relative to previous sidescan images. Further, in this work there is no need for a flat bottom assumption in order to disambiguate the sidescan sonar returns, as expected signals are generated from a bathymetry map and projected into the sidescan sonar time of flight domain, which is an unambiguous mapping.

III. Method

For TRN, a measurement model must be defined that allows the correlation of a measurement to an expected measurement. The correlation methods presented in this paper detect acoustic shadows in the measured sidescan sonar signal and correlate them with expected shadows. Expected shadows are generated for a given pose estimate with respect to a stored terrain map by first extracting a bathymetry profile along the scan plane from the terrain map. Occluded terrain points are

identified in the profile according to line of sight from the sonar transducer, and these points are projected into the time of flight domain to generate expected shadows by the following relation:

$$\tau = \frac{2r}{c} \tag{1}$$

where τ is the time of flight, r is the range from the sonar transducer to the terrain point and c is the local speed of sound estimate. Measured shadows are identified by simple intensity thresholding, where the threshold used in this work is 0.7 of the maximum return intensity. Figure 3 provides an example of scan plane bathymetry profile extraction, expected shadow generation, and identification of a measured shadow using AUV field data. It should be noted that all intensity values for the sidescan sonar data presented in this paper are the logarithms of the raw sidescan intensity returns.

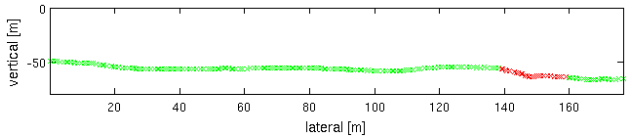

(a) Sidescan plane bathymetry terrain profile

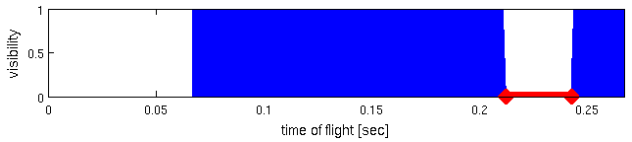

(b) Expected visibility in time of flight domain

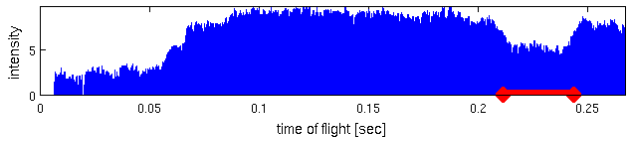

(c) Sidescan sonar measurement

Figure 3: Measured and expected acoustic shadow identification. (a) Bathymetry terrain points along sidescan scan-plane. Red points are occluded according to line of sight from sonar transducer. (b) Expected visibility in the time of flight domain for a given pose estimate. Expected acoustic shadows are identified in red. (c) Sidescan measurement, with identified acoustic shadows identified in red. Note: the vertical alignment of the top figure bathymetry occlusions with the time of flight occlusions is incidental; for example, were the altitude different, this alignment would not be preserved, and in general should not be expected.

The alignment of expected and measured acoustic shadows drives measurement weighting, which is used in non-parametric filtering (e.g. particle filter or point mass filter) to determine the confidence in a given pose estimate. For each pose estimate, expected shadows are generated and correlated against measured shadows.

Two correlation methods were developed and tested. The first is an XOR correlation method that treats all shadows with equal confidence according to line of sight geometry. The second method weights expected shadows differently based on how occluded a given terrain point is, according to what the authors have termed "differential height". The details of each method are presented below.

A. XOR Correlation

The basis of the XOR correlation method lies in rewarding shadow alignment, and penalizing shadow misalignment. The time of flight domain is binned in the range $[\tau_{min}, \tau_{max}]$ into K bins. The maximum time considered, τ_{max}, corresponds to the maximum time of flight measured by the sidescan sonar sensor. The minimum time considered, τ_{min}, was set as a multiple of the altitude in order to rule out the minimum range being measured as a "shadow". In this work that multiple of altitude was set to 1.4.

A flat misalignment probability α is assigned when an XOR condition is satisfied for which there is shadow aligned with non-shadow. For this work, $\alpha = 0.48$. The measurement weight for a given pose estimate i for timestep t, w_i^t, is then the product of all individual measurement contributions over all K time of flight bins. The measurement contribution is either α, if there is shadow misalignment, or $(1-\alpha)$ when either shadow or non-shadow are aligned, as given by the following equation:

$$w_t^i = \prod_{k=1}^{K} \underbrace{1\{e_k \oplus m_k\}}_{\text{misalignment}} \alpha + \underbrace{(1 \oplus 1\{e_k \oplus m_k\})}_{\text{alignment}} (1-\alpha)$$

where

$$e_k = \begin{cases} 0 & \textbf{expected} \text{ shadow} \\ 1 & \text{otherwise} \end{cases}$$

$$m_k = \begin{cases} 0 & \textbf{measured} \text{ shadow} \\ 1 & \text{otherwise} \end{cases} \tag{2}$$

where $\oplus$ denotes an XOR operation. For numerical reasons, due to the large value of K, these weights are evaluated as sum of log weights over the K bins, and then the sum is exponentiated in order to arrive at the measurement weight for the pose i and timestep t.

B. Differential Height Correlation

Some expected shadow assignments are more likely than others based on the pose estimate and the terrain map. A slight grazing occlusion should be trusted less than the occlusion expected behind a large mound.

One way to quantify the confidence in expected shadow assignments is by the calculation of "differential heights". For terrain point m in the scan plane of pose estimate i, a differential height value, δz_m^i, is calculated that reflects how occluded or visible the terrain point is. Figure 4 illustrates the meaning of differential height.

If the point is occluded according to line of sight from the sonar transducer, the differential height is the terrain height difference at point m necessary to make the point visible, and this value is negative. Similarly, if the point is visible according to line of sight, its differential height is the terrain height difference necessary to make it occluded, and this value

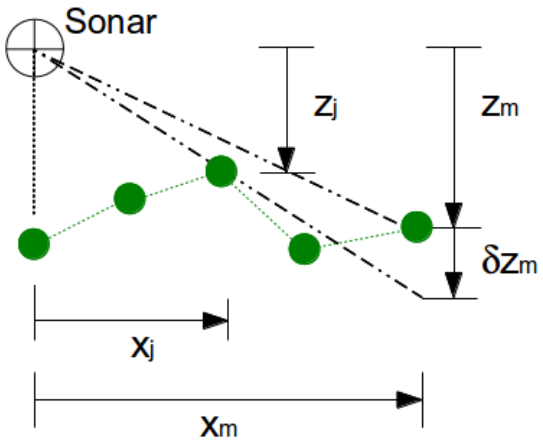

Figure 4: Differential height diagram. Shown is the differential height necessary to make a visible terrain point, m, occluded. Terrain points shown in green.

is positive. Equation 3 provides the definition of differential height.

$$\delta z_m^i = \min_j \ (x_m \frac{z_j}{x_j} - z_m), \forall j = 1, 2, \ldots, m-1 \qquad (3)$$

In order to translate differential heights into probabilities, the differential height values are passed through a sigmoid function, given by the following relation:

$$p_m = 0.5 + \lambda \frac{\delta z_m - \mu}{\sqrt{\gamma^2 + (\delta z_m - \mu)^2}} \qquad (4)$$

where p_m is the probability that terrain point m is visible, μ shifts the mean differential height, and γ and λ adjust the sigmoid shape. For the results presented in this work, $\mu = -1, \gamma = 1, \lambda = 0.1$. Shifting the mean differential height by μ accounts for the observed behavior that expected shadows are overly predicted by pure line of sight when compared to measured shadows. Further, the λ value of 0.1 is chosen rather than the full possible value of 0.5 in order to account for measurement uncertainty as a means to prevent filter overconfidence, as detailed in [9]. Figure 5 provides a plot of the sigmoid given by Equation 4.

Once differential heights have been calculated for each terrain point in the scan plane, these values are projected into the time of flight domain, according to the relation given by Equation 1, and linearly interpolated in order to obtain a differential height function in the time of flight domain.

The measurement weight for a given pose estimate i for timestep t, w_i^t, is given by:

$$w_t^i = \prod_{k=1}^{K} \underbrace{1\{m_k = 1\}}_{\text{measured visible}} P_k^i + \underbrace{1\{m_k = 0\}}_{\text{measured shadow}} (1 - P_k^i) \qquad (5)$$

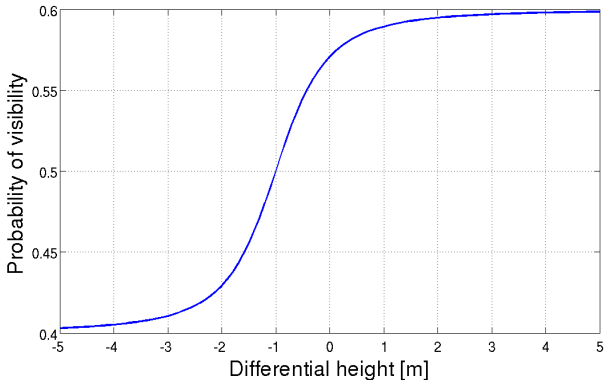

Figure 5: Sigmoid function given by Equation 4 with parameters $\mu = -1, \gamma = 1, \lambda = 0.1$

where P_k^i is the probability of visibility for time of flight bin k and pose estimate i obtained from the differential height method.

C. Non-parametric Filter

This work is intended for use with non-parametric navigation filters. Examples of such filters include particle filters and point mass filters (PMFs), both of which are extensively used in AUV navigation solutions, and detailed in [10]. For this work, a PMF was chosen for its ease of implementation.

For simplicity, the PMF estimated state is 2-D north and east vehicle position $\mathbf{x} = [x_N, x_E]^T$. A grid of discrete state hypotheses was instantiated about a nominal position.

For each timestep, an estimate mean and covariance are evalulated by:

$$\hat{\mathbf{x}} = \sum_{i=1}^{N_N} \sum_{j=1}^{N_E} \begin{bmatrix} x_N(i) \\ x_E(j) \end{bmatrix} w^{(i,j)} \qquad (6)$$

$$\Sigma_x = \sum_{i=1}^{N_N} \sum_{j=1}^{N_E} (\begin{bmatrix} x_N(i) \\ x_E(j) \end{bmatrix} - \hat{\mathbf{x}})(\begin{bmatrix} x_N(i) \\ x_E(j) \end{bmatrix} - \hat{\mathbf{x}})^T w^{(i,j)} \qquad (7)$$

where $w^{(i,j)}$ is the weight for cell (i, j) of the point mass filter.

IV. Experimental Results

Results were obtained using field data from Monterey Bay Aquarium Research Institute (MBARI) *Dorado*-class AUV runs that demonstrate the feasibility of sidescan sonar as a sensor for TRN. The field data was collected in the Gulf of California. The vehicle was outfitted with a Kearfott SeaDevil INS/DVL, along with a Reson 7125 200 kHz multibeam sonar and Edgetech 110 kHz chirp sidescan sonar. Data was obtained through the use of MB-System software [11].

Figure 6 is a result for a run of roughly 500m distance travelled. This dataset comprises the mapping run used to generate the bathymetry map, and thus the "Mapping Trajectory" shown in Figure 6 is assumed to be truth. The bathymetry map is a 1-meter resolution digital elevation map (DEM).

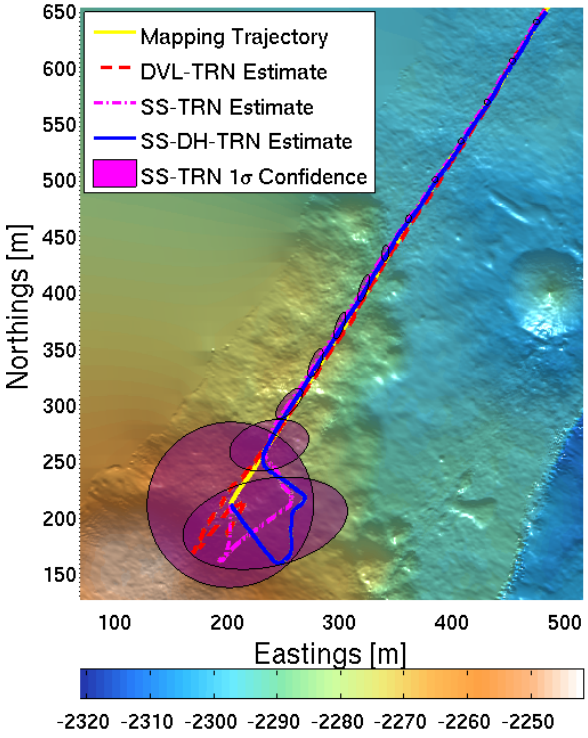

(a)

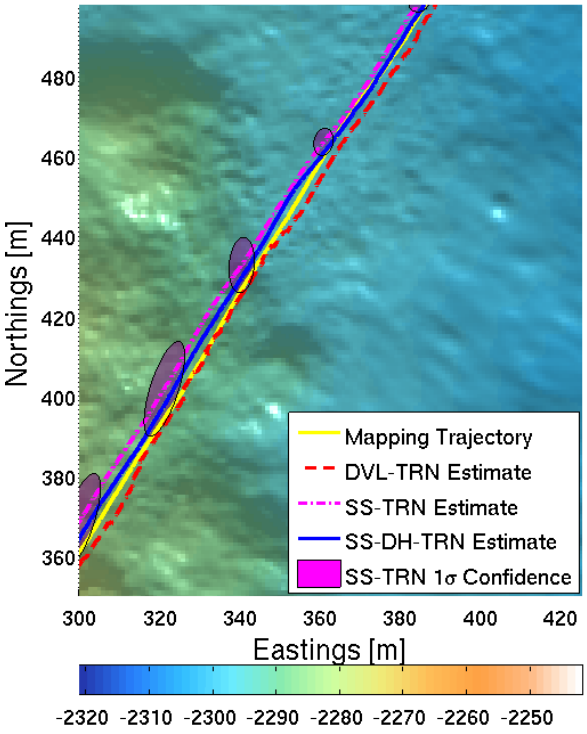

(b)

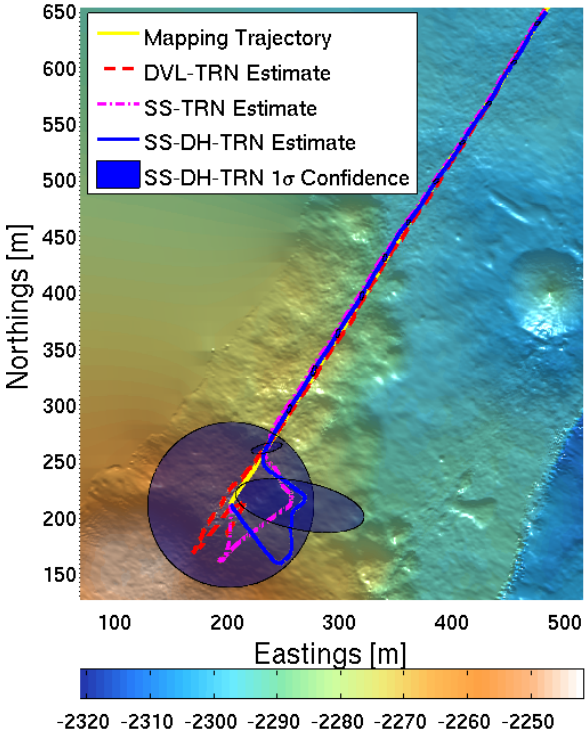

(c)

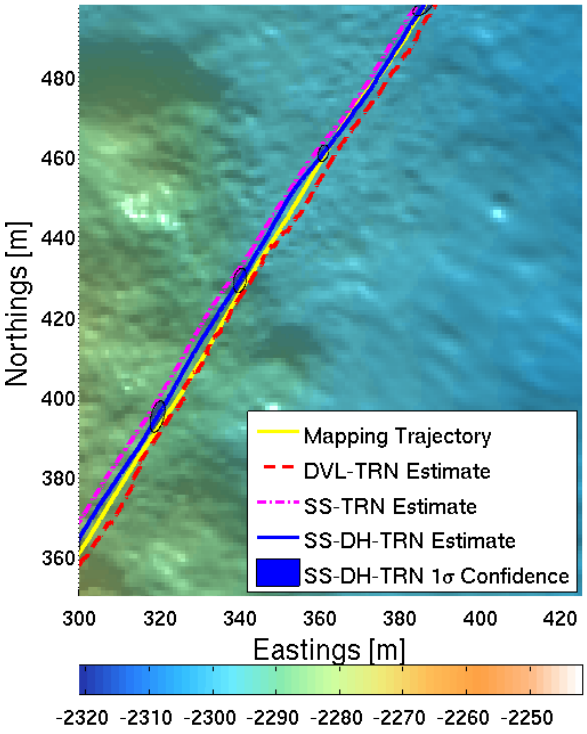

(d)

Figure 6: Terrain-relative navigation estimates on Gulf of California dataset using sidescan sonar XOR correlation (SS-TRN), sidescan sonar differential height method (SS-DH-TRN), and standard TRN (DVL-TRN) for a field trial. Mean estimate tracks shown on all plots. (a) Full track, SS-TRN covariance ellipses plotted. (b) Zoomed in on converged region with SS-TRN covariance ellipses plotted. (c) Full track, SS-DH-TRN covariance ellipses plotted. (d) Zoomed in on converged region with SS-DH-TRN covariance ellipses plotted.

The area of terrain shown in Figure 6 contains good topographical information directly beneath the AUV trajectory, as well as to the starboard side of the trajectory, and as such enables a fair comparison of the relative performance of DVL-based TRN and sidescan sonar-based TRN methods.

Shown in Figure 6 is the point-mass-filtered trajectory estimate obtained through correlation of sidescan sonar to the bathymetry map using the XOR correlation method (*SS-TRN*), along with the independent estimate obtained through the differential height method (*SS-DH-TRN*). For each method, a point mass filter was run with a discrete grid 250m by 250m with 5m spacing in north and east directions. Each grid cell location was propagated in time according to the north-east changes from the mapping trajectory. For comparison, the TRN estimate obtained through standard DVL-based TRN (*DVL-TRN*) is also plotted in Figure 6. It should be noted that the SS-TRN and SS-DH-TRN estimates were obtained independently of each other and of the DVL-TRN estimate, i.e. no sensor fusion was exploited for these estimates.

The convergence of the SS-TRN and SS-DH-TRN estimates highlights the promise of the presented correlation methods for TRN. The SS-DH-TRN mean estimate converges closer to the mapping trajectory than the SS-TRN mean estimate, as shown in Figure 6. Further, tighter covariance ellipses are observed for SS-DH-TRN than for SS-TRN. Figure 7 presents the standard deviations for DVL-TRN, SS-TRN, and SS-DH-TRN estimates, showing that the sidescan sonar-based estimators have confidence in the range of the DVL-based estimator once converged, though the sidescan sonar-based estimators take longer to converge.

The behavior of the sidescan sonar-based filters in the above results can be explained with the help of Figure 8 by observing terrain features starboard of the vehicle path. Shown in Figure 8 is the terrain map with the mapping trajectory plotted, along with the sidescan sonar signals stitched together over the run into an image. There are two major shadow areas visible. The upper acoustic shadow region is generated by a large mound located roughly 125m starboard of the vehicle track. This is a large feature that produces a strong shadow region. The lower acoustic shadow region is caused by a more subtle topographical change. This region occurs due to a gradual downward slope starboard of the vehicle that produces a grazing occlusion. The appearance of the acoustic shadow region from this less substantial feature is exciting for the prospect of using sidescan sonar for TRN, as it demonstrates that large terrain features (e.g. mounds) are not required for strong shadows to be observed.

Figure 9 shows the alignment of expected shadows to measured shadows for the SS-TRN Maximum Likelihood (ML) PMF grid cell using the XOR correlation method. The alignment is not perfect, but the expected shadows do align qualitatively well with the measured shadows. The slight misalignment can be attributed to a number of factors, including the fact that the simplified sensor model employed in this work does not fully capture the complex physics of acoustic propagation and sidescan sonar dynamics.

Differential heights and the visibility probabilities derived from differential heights are shown in Figure 10 for the SS-DH-TRN ML pose estimate. As detailed in Section III-B,

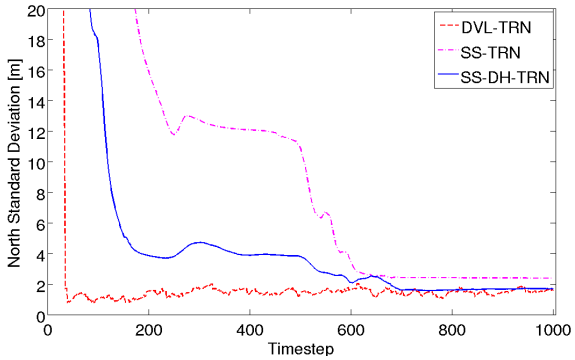

(a) North standard deviations

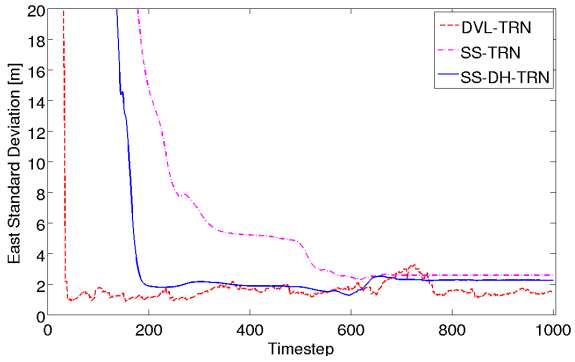

(b) East standard deviations

Figure 7: Standard deviations for DVL-TRN, SS-TRN, and SS-DH-TRN estimators.

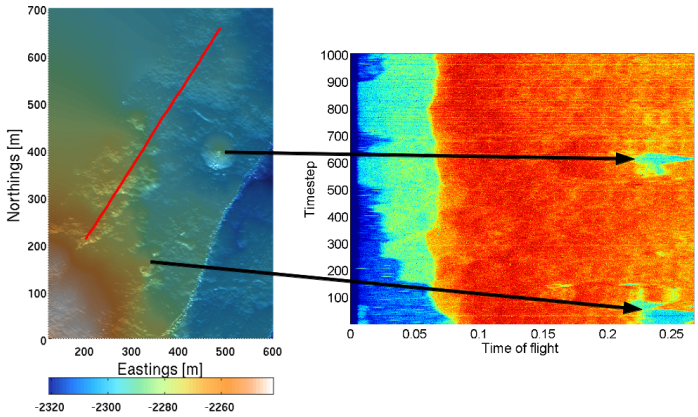

Figure 8: Terrain features leading to acoustic shadows in sidescan sonar signal. (Left) Terrain map with mapping trajectory plotted in red. (Right) Acoustic shadows in sidescan sonar signal identified. The lower shadow region results from a downward slope starboard of the vehicle. The upper shadow region results from a large mound starboard.

the mean differential height value was shifted by 1 meter ($\beta = 1$ from Equation 4), and the probabilities are biased toward higher visibility, as seen by the fact that probabilities for differential heights near zero are not centered about 0.5.

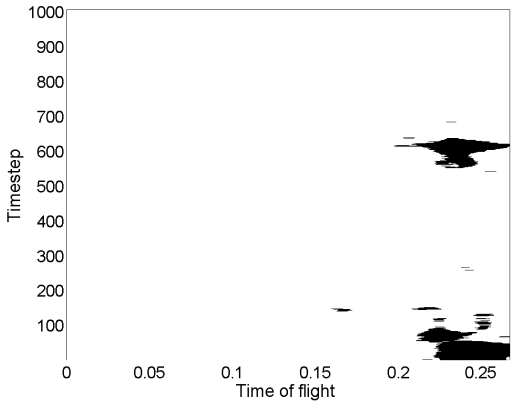

(a) Measured acoustic shadows

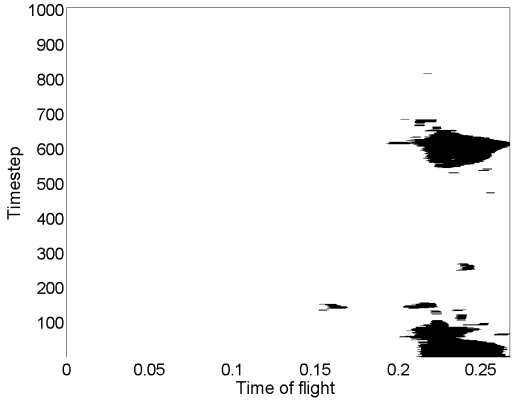

(b) Expected acoustic shadows in ML pose estimate

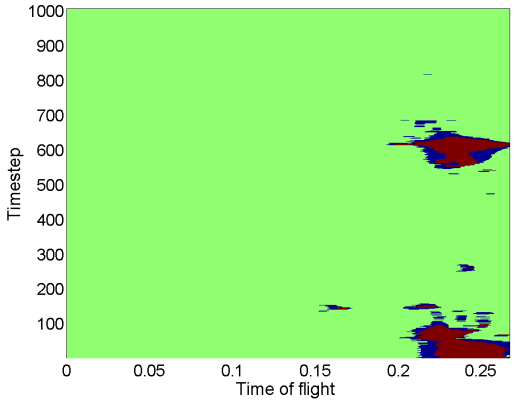

(c) Shadow alignment between measured and expected images

Figure 9: Measured and expected acoustic shadows. The measured acoustic shadows are large drops in intensity, and are extracted by thresholding. The expected shadow signal is for the SS-TRN Maximum Likelihood (ML) PMF pose cell. The bottom plot shows alignment between expected and measured shadows. Green indicates visibility alignment between the measured and expected signal. Red indicates shadow alignment between the measured and expected signal. Blue indicates misalignment.

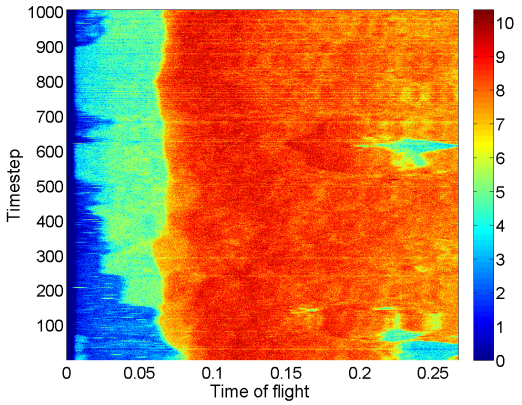

(a) Sidescan sonar image

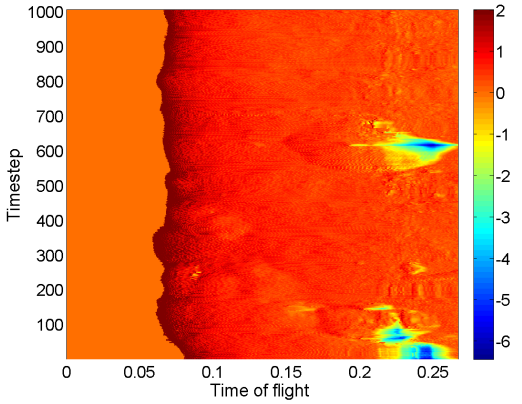

(b) Differential height image for MLE pose estimate

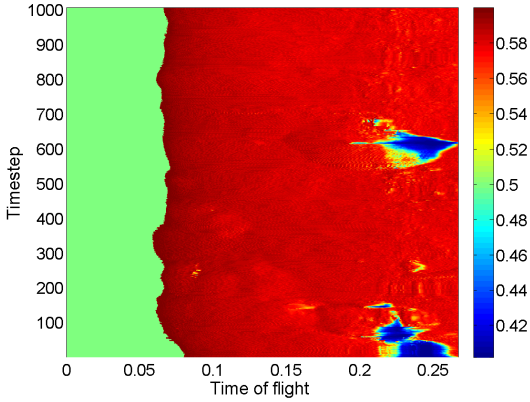

(c) Visibility probability image for MLE pose estimate

Figure 10: Differential heights and probabilities for SS-DH-TRN Maximum Likelihood (ML) PMF pose cell. (a) Sidescan sonar intensity image. (b) Differential height image, values in meters. Blue indicates more negative differential heights, red indicates more positive differential heights. (c) Probability image derived from differential heights, passed through the sigmoid function given by Equation 4. Blue indicates lower probability of visibility (more probable shadow), red indicates more probable visible return.

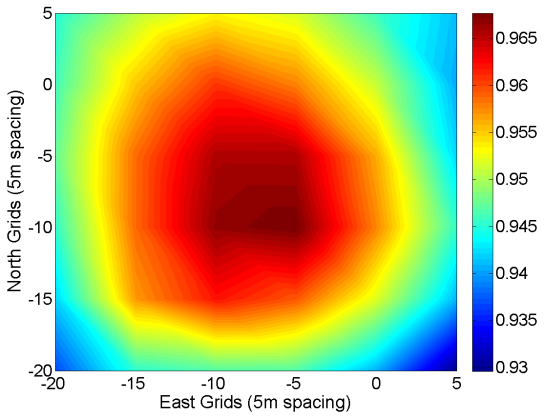

(a)

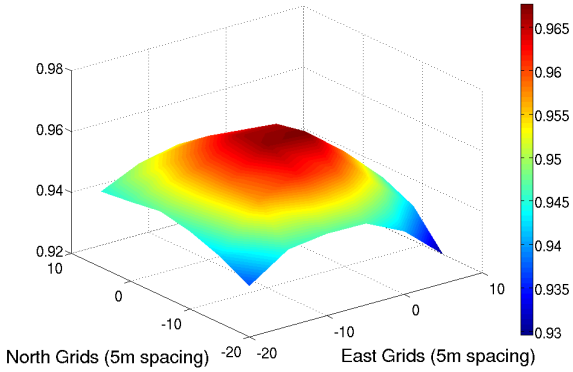

(b)

Figure 11: SS-TRN PMF correlation peak about the mapping position (0,0). Red indicates higher correlation. The plots show that the correlation peak is offset from the mapping position by roughly 10m, where this 10m is along the vehicle path.

A. *Along-Track Estimate Offset*

An issue with the results presented is an offset along track in the estimated mean positions relative to the mapping position. While it is clear that the estimators are converging to the mapping trajectory as shown in Figure 6, the estimated mean positions, once converged, trail the mapping position by roughly 10 meters. This behavior can be observed by the correlation peak offset from the origin for the SS-TRN estimate, given by Figure 11, where the origin is the mapping position.

There are several potential contributors to this along-track offset. For example, there is the possibility of a timing offset or lag in recording sidescan sonar data relative to the mapping data. As the sidescan sonar data was processed on a separate computer the possibility of a timing issue is real. Additionally, there may be a contribution to the offset coming from a pitch bias between the sidescan sonar transducer and the multibeam sonar. Identifying the cause(s) of this along-track offset is the subject of current work.

V. Conclusion

This paper demonstrated the feasibility of non-interferometric sidescan sonar as a sensor for TRN. Navigation results were presented using AUV field data that demonstrated TRN performance using sidescan sonar data comparable to traditional DVL-TRN performance in a terrain area where there was good information available to both sensing modalities.

As future work, more datasets will be processed to explore the performance benefit of incorporating sidescan sonar data into TRN over varied terrain. In particular, the collection of field data over terrain where DVL-based TRN experiences accuracy degradation (i.e. locally flat terrain) is planned, as the ultimate goal of this work is to augment TRN accuracy with sidescan sonar data in such terrain regions.

Acknowledgment

The authors thank the Monterey Bay Aquarium Research Institute (MBARI) for all data and the opportunity to test results at sea. In particular, the authors thank Dave Caress for his valuable assistance with MB-System. Jose Padial is supported by NASA National Space Technology Research Fellowship NNX11AM92H. Shandor Dektor has received support from a National Defense Science and Engineering Graduate Fellowship and a Stanford Graduate Fellowship.

References

[1] D. Meduna, *Terrain relative navigation for sensor-limited systems with application to underwater vehicles*. Phd, Stanford University, August 2011.

[2] S. Dektor and S. Rock, "Improving robustness of terrain-relative navigation for AUVs in regions with flat terrain," in *Autonomous Underwater Vehicles (AUV), 2012 IEEE/OES*, pp. 1 –7, September 2012.

[3] O. Hagen, K. Anonsen, and T. Saebo, "Low altitude auv terrain navigation using an interferometric sidescan sonar," in *OCEANS 2011*, pp. 1 –8, sept. 2011.

[4] S. Reed, Y. Petillot, and J. Bell, "A model based approach to mine detection and classification in sidescan sonar," in *OCEANS 2003 MTS/IEEE: CELEBRATING THE PAST...TEAMING TOWARD THE FUTURE*, pp. 1402–1407, 2003.

[5] J. Bell, *A Model for the Simulation of Sidescan Sonar*. PhD thesis, Heriot-Watt University, 1995.

[6] S. Stalder, H. Bleuler, and T. Ura, "Terrain-based navigation for underwater vehicles using side scan sonar images," in *Oceans 2008*, vol. 1-4, pp. 51–53, 2008.

[7] M. F. Fallon, M. Kaess, H. Johannsson, and J. J. Leonard, "Efficient AUV navigation fusing acoustic ranging and side-scan sonar," in *ICRA*, pp. 2398–2405, 2011.

[8] I. Ruiz, Y. Petillot, and D. Lane, "Improved AUV navigation using side-scan sonar," in *OCEANS 2003 MTS/IEEE: CELEBRATING THE PAST...TEAMING TOWARD THE FUTURE*, pp. 1261–1268, 2003.

[9] S. Thrun, W. Burgard, and D. Fox, *Probabilistic Robotics*. Intelligent Robotics and Autonomous Agents, MIT Press, 2005.

[10] K. Anonsen and O. Hallingstad, "Terrain aided underwater navigation using point mass and particle filters," in *Position, Location, And Navigation Symposium, 2006 IEEE/ION*, pp. 1027–1035, 2006.

[11] D. W. Caress and D. N. Chayes, "Mb-system: Mapping the seafloor, http://www.mbari.org/data/mbsystem and http://www.ldeo.columbia.edu/res/pi/mb-system," 2006.